Hybrid Organic/Inorganic Nanostructures for Highly Sensitive Photoelectrochemical Detection of Dissolved Oxygen in Aqueous Media

Sebastiano Bellani, Ali Ghadirzadeh, Laura Meda, Alberto Savoini, Alessandra Tacca, Gianluigi Marra, Rui Meira, Jorge Morgado, Fabio Di Fonzo, and Maria Rosa Antognazza**

Precise, reliable, and remote measurement of dissolved oxygen in aqueous media is of great importance for many industrial, environmental, and biological applications. In particular, photoelectrochemical sensors working in differential mode have recently demonstrated promising properties, in terms of stability, sensitivity, and application potential. Here, a new approach is presented, combining visible light sensitivity, efficient photocurrent generation, and solution-processed fabrication methods of conjugated polymers, with charge carriers selectivity, energetic alignment favorable to efficient interfacial charge transfer and high surface area achievable by using metal oxide nanostructures. Extensive characterization and optimization of the hybrid organic/inorganic system are carried out, leading to the realization of an oxygen sensor device, based on nanostructured palladium oxide/poly[(9,9-dioctylfluorenyl-2,7-diyl)-*alt*-5,5-(4′,7′-di-2-thienyl-2′,1′,3′-benzothiadiazole]/[6,6]phenyl-C61-butyric acid methyl ester (PdO/APFO-3:PCBM) as materials of choice. State-of-the-art sensitivity, amounting at −5.87 μA cm^{-2} ppm^{-1}, low background signal, in the order of −4.85 μA cm^{-2}, good electrochemical stability for more than 2 h of continuous functioning and high reproducibility of the signal over the pH 1 to 10 range, are reported, making the hybrid device suitable for several practical uses. The results fully validate the mixed organic/inorganic approach for photoelectrochemical applications, and pave the way for its further exploitation in fields like waste water treatment, environmental monitoring, and water splitting.

1. Introduction

The measurement of oxygen content in aqueous media solution phase is of great importance for many industrial, environmental, and biological applications. Most common dissolved oxygen sensors include Clark electrodes, aqueous electrochemical cells, and optical sensors.[1–4]

A Clark electrode is composed by a cathode and an anode submersed in an electrolyte. Oxygen enters the sensor through a permeable membrane by diffusion and is reduced at the cathode, giving rise to a measurable electrical current, which is proportional to the oxygen concentration itself. Electrochemical sensors widened this scheme, originally proposed by Clark in 1956, and include now polarographic and galvanic sensors (requiring and not requiring an external bias, respectively).

Optical methods are based on the use of specific chemical dyes, whose photoemission efficiency is strongly affected by the presence of oxygen, accordingly to the well-known Stern–Volmer equation. In this approach, the measurement of photoluminescence intensity

S. Bellani, Dr. A. Ghadirzadeh, Dr. F. Di Fonzo, Dr. M. R. Antognazza
Center for Nano Science and Technology @PoliMi
Istituto Italiano di Tecnologia
Via Pascoli 70/3, 20133 Milano, Italy
E-mail: fabio.difonzo@iit.it; mariarosa.antognazza@iit.it
S. Bellani
Politecnico di Milano
Dip.to di Fisica
P.zza L. da Vinci 32, 20133 Milano, Italy
Dr. A. Ghadirzadeh
Politecnico di Milano
Dip.to di Energia
P.zza L. da Vinci 32, 20133 Milano, Italy
Dr. L. Meda, Dr. A. Savoini, A. Tacca, G. Marra
Istituto Eni Donegani
Dip.to Chimica-Fisica
Via Giacomo Fauser 4, 28100 Novara, Italy
Dr. R. Meira, Prof. J. Morgado
Department of Bioengineering
Instituto Superior Técnico
University of Lisbon and Instituto de Telecomunicações
Avenida Rovisco Pais 1, 1049-001 Lisboa, Portugal

DOI: 10.1002/adfm.201500701

and/or lifetime gives a direct, sensitive, and reliable measurement of dissolved oxygen concentration values.

Photoelectrochemical detection is a newly developed and promising method,[5,6] in which light is used to excite active species (mainly transition metal complexes) at the electrode surface, and the detection signal is constituted by the generated photocurrent. In this case, the measured signal (i.e., the current density) is related to the intensity of exciting light, to the intrinsic properties of the light-absorbing materials, to the type and shape of electrodes, to the eventually applied bias, and to the composition of the electrolyte. Photoelectrochemical detection can in principle exploit the advantages of both electrochemical and optical techniques, offering good selectivity, portability, and possibility of miniaturization and integration, like in the case of optical methods, but at a lower cost.

In addition, photoelectrochemical sensors allow, by working in differential mode, for overcoming the need of frequent recalibration, a major disadvantage of most electrochemical systems, and can enable measurements in all cases where continuous monitoring is needed. Moreover, the decoupling between excitation (light) and detection (current), in a complementary approach respect to existing optical methods, and the use of differential measurements, permit to reduce the background signals respect to standard electrochemical sensors, and to increase overall sensitivity. Till now, however, few works have been reported on the implementation of new materials and device architectures.[5–8] In this scenario, hybrid organic–inorganic systems are considered here, and the advantages of the simultaneous utilization of both components (namely, solution processability, and visible light absorption, typical of conjugated polymers, on one side; stability, well-controlled morphology and electrical transport, characteristic of metal oxides, on the other side) are exploited. Nowadays, organic semiconductors technology is well established in many industrial applications, including light emitting diodes (LED), field effect transistors (FET), and photovoltaic (PV) devices.[9] More recently, many reports fully demonstrated the real possibility to integrate conjugated polymers in sensors for biomedical and neuroscience applications, as well as in several types of electrochemical cells.[10,11] In particular, thiophene-based derivatives proved to be biocompatible, to preserve their optoelectronic properties in an aqueous environment, to work in acidic and basic conditions with reasonable electrochemical stability.[12–19] Several conducting polymers, including polyaniline,[20] polypyrrole,[21] and polythiophene derivatives,[6,22] have shown good electrocatalytic activity for oxygen reduction, making them promising candidates for the realization of electrochemical oxygen sensors. However, reduced photocurrent densities (in the order of few μA cm $^{-2}$ upon approximately 100 mW cm^{-2} photoexcitation density) and poor electrical transport reduces the overall efficiency of devices based exclusively on the use of semiconducting conjugated polymers.

For this reason, photoactive organic layers are coupled here to oxide nanostructures, and in particular to palladium oxide (PdO). PdO is a high work function, p-type semiconductor, which makes it suitable for working as a hole selective contact in a hybrid device.[23,24] In addition, PdO offers high insolubility, good thermal stability, non-toxicity as well as corrosion resistance in a wide range of pH values, from acid to basic conditions. Moreover, it is cheaper than other metal oxides with similar characteristics, such as IrO_2 and PtO.[25–27] In this work, after extensive screening among different polymers already studied for PV solar cells, we realize an hybrid photoelectrochemical sensor for dissolved oxygen, based on poly[(9,9-dioctylfluorenyl-2,7-diyl)-*alt*-5,5-(4′,7′-di-2-thienyl-2′,1′,3′-benzothiadiazole] (APFO-3):[6,6]phenyl-C61-butyric acid methyl ester (PCBM), as the light sensitive and charge generating layer. APFO-3:PCBM bulk heterojunction is then efficiently coupled to a nanostructured PdO electrode, which offers enhanced charge collection efficiency and high surface area available for catalysis. State-of-the-art sensitivity, good electrochemical stability and high reproducibility in different environmental conditions, ranging from acid to basic pH, are reported, making the hybrid device suitable for several different applications.

2. Results and Discussion

2.1. Polymer Photocatalytic Activity

As a first step, several different conjugated polymers were screened for their photoelectrochemical activity in aqueous environment towards oxygen reduction. Polymer thin films were deposited on FTO-covered glass substrates, thus realizing a monolithic photovoltaic/photocatalytic electrode. Device architecture, polymer chemical structures, and polymer blend (polymer:PCBM) absorbance spectra are reported in **Figure 1**,

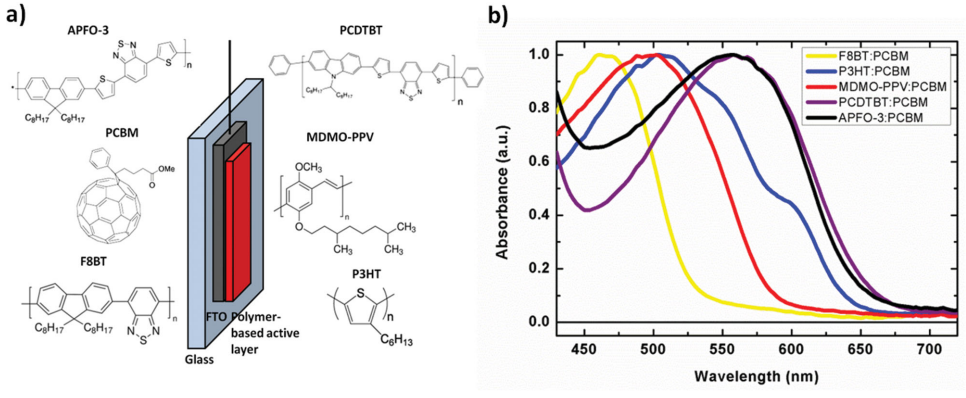

Figure 1. a) Schematic representation of monolithic photovoltaic/photocatalytic electrodes. b) Thin film normalized absorbance spectra of the different blends.

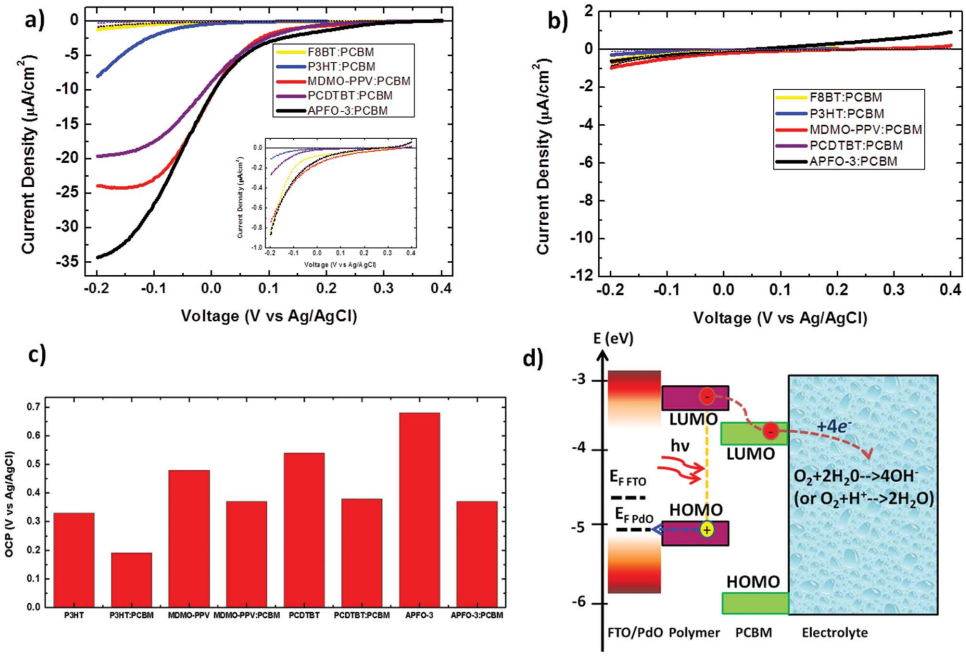

Figure 2. a) Linear scan voltammetry of blended materials under dark (dot lines) and under 1 SUN illumination (solid lines) in PBS at pH 7. The inset shows a enlargement of the dark currents. b) Linear scan voltammetry of the same blend in deoxygenated solutions. c) Open-circuit potential (OCP) for the selected photocatalytic materials, in the pristine and blended forms. d) Schematic representation of the energetic levels of the systems and the photocatalytic activity mechanisms. The position of the conduction and valence band in PdO is approximate, since the electronic structure is still under debate;[38] the PdO work function was experimentally measured by KPM.

reflecting many possible choices of different materials all over the visible light spectral window. Absorbance spectra of the pristine polymer are also reported in Figure S1 (Supporting Information).

Figure 2a reports the linear scan voltammetry (LSV) in dark and upon light (1 SUN) for polymer:PCBM bulk heterojunctions, in phosphate buffered saline (PBS) solution at pH 7, in open air conditions. In all cases, a photocurrent signal is observed, clearly indicating the occurrence of photoelectrochemical reactions sustained by the polymer, in accordance with previous, similar reports on polymer-based photoelectrochemical cells.[12,13] The largest photocurrent densities were obtained in APFO-3:PCBM films; conversely, poly[(9,9-di-n-octylfluorenyl-2,7-diyl)-*alt*-(benzo[2,1,3]thiadiazol-4,8-diyl)] (F8BT)-based films resulted in the lowest photocurrent densities among considered cases, and they will not be further considered in the following analysis. Figure 2b presents the LSV in the same materials, but upon oxygen removal from PBS solution (upon continuous nitrogen purging for 30 min, a residual dissolved oxygen concentration was measured by a commercial oxygen sensor, amounting at approximately 0.2 mg L^{-1}). In all cases, photocurrent density is significantly reduced to values in the order of few μA per cm^2, by reduction factors approximately ranging between 20 and 50; such residual photocurrent could be due to hydrogen evolution, as already verified for the case poly(3-hexylthiophene-2,5-diyl) P3HT:PCBM,[12,13] or to other species, including a few amount of oxygen, still present in the electrolyte. This phenomenon demonstrates however the key-role played by dissolved oxygen in establishing the measured current, possibly indicating photoelectrochemical activity towards oxygen reduction reaction (ORR) sustained by the conjugated polymer in contact with the aqueous electrolyte. Similar results were observed also by using pristine polymers (without PCBM) as photoactive materials (Figure S2, Supporting Information), but in this case recorded photocurrent densities were reduced up to five times, in accordance with much lower charge dissociation efficiency. Figure 2c shows the open circuit potential (OCP) for the considered photocatalytic materials in the pristine and blended forms. It is worth to note that the highest OCP values, obtained in particular for MDMO-PPV (0.48 V vs Ag/AgCl), PCDTBT (0.51 V vs Ag/AgCl) and APFO-3 (0.67 V vs Ag/AgCl), allow photocathodic activity also at very high voltages with respect to best noble metal-based electrocatalysts reported for oxygen reduction.[28] While the highest photocurrents are obtained by employing a bulk heterojunction configuration, OCP values recorded in polymer blends are reduced in all cases with respect to the case of pristine polymers. A possible photoelectrocatalytic mechanism, able to explain both higher photocurrent generation efficiency (in presence of oxygen), and OCP reduction recorded in polymer blends as compared to pristine polymers, is proposed in Figure 2d and in the **Scheme 1**.

Excitonic states generated in the polymer blend upon illumination undergo fast and efficient bulk dissociation, and

A) $P3HT + \hbar\nu \rightarrow P3HT^*$

B) $P3HT^* + PCBM \rightarrow P3HT^+ + PCBM^-$

C1') $4PCBM^- + O_2 + 4H^+ \rightarrow 4PCBM + 2H_2O$ in acid conditions, or:

C1'') $4PCBM^- + O_2 + 2H_2O \rightarrow 4PCBM + 4OH^-$ in basic conditions

C2) $P3HT^+ + FTO\ (PdO) \rightarrow P3HT + FTO^+\ (PdO^+)$

Scheme 1. Photoelectrocatalysis mechanism of ORR by polymer blends.

subsequently free charges migrate towards the electrodes. In particular, in accordance with the sign of the photocurrent, electrons move towards the electrolyte, where give rise to oxygen reduction reactions, while holes are preferentially (but not selectively) collected at the FTO electrode. Conversely, in the case of the pristine polymer, dissociation can occur only at the interfaces (FTO/polymer and polymer/electrolyte), and the large majority of photogenerated excitons are lost due to recombination before they can reach the interface with the electrolyte and give rise to ORR (the average exciton diffusion length in polymers is reported to be approximately 10 nm).[29–31] Regarding OCPs, this is expected to decrease in the case of the blends due to the lower energy of the lowest unoccupied molecular orbital (LUMO) of PCBM ≈ 4.3 eV) with respect to the polymer ones (around 3–3.5 eV). For these reasons, in order to find the most efficient photoactive polymer for oxygen sensing, it is necessary to achieve a good compromise between charge generation and dissociation capability, and OCP value.

Moreover, aiming at the realization of a photoelectrochemical dissolved oxygen sensor of practical use, it is also necessary to achieve high sensing performances. Toward this goal, we coupled the conjugated polymer blend to an array of hierarchical metal oxide nanostructures, introduced on top of the FTO contact. The advantage of the proposed approach is twofold: (i) having a hole-selective contact, thus maximizing the charge collection efficiency at interfaces (see energetic scheme in Figure 2d), and (ii) increasing the contact area between the polymer and the charge-selective oxide as well as between the polymer and the electrolyte, thus increasing the density of active sites available for ORR at the interface with the electrolyte. The photocurrent onset voltage is also expected to be shifted towards higher values,[32] thus enabling to efficiently operate in a voltage window in which all employed materials are stable and avoiding degradation effects (i.e., cathodic reduction of the metal oxide toward metallic state), with a clear advantage also on overall stability.

2.2. Nanostructure Characterization and Optimization

Among all possible choices, we selected PdO due to its unique physicochemical properties. PdO is a p-type semiconductor with a bandgap in the range between 1.5 and 2 eV, depending on the crystallinity degree,[24,25] highly insoluble in water and thermally stable up to 750 °C (at which it decomposes into palladium and oxygen).[26] It is a nontoxic and environmental friendly oxide and moreover it offers good stability in a wide range of pH, from acid to basic, as shown by Pourbaix diagrams in literature.[25,33] Pulsed laser deposition (PLD) has been chosen as the deposition technique, since this is a versatile physical vapor deposition route for growing arrays of nanostructures with controlled properties, including composition, surface area, porosity, thickness, and oxidation state.[34] Moreover, it has been previously demonstrated the formation of noble metal oxides by this technique.[35,36] By independent control of deposition parameters, like background gas pressure, target to substrate distance and laser fluence, it is possible to tune kinetic energy, directionality, and size of the generated atom clusters. In a particular window of parameters,[37]

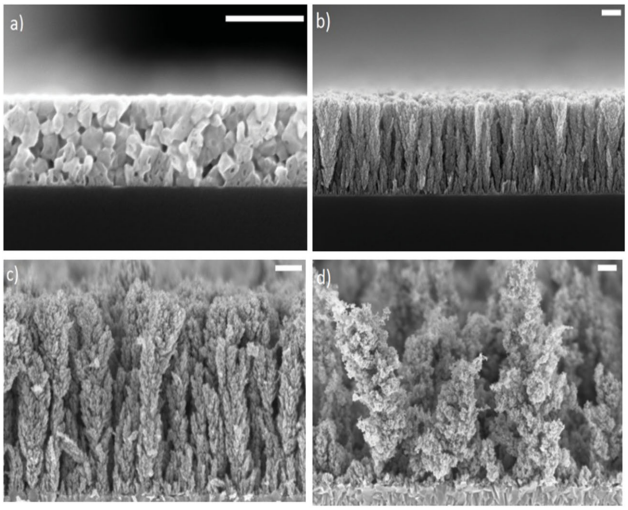

Figure 3. Effect of pressure on morphology. Crosssection SEM images of PdO deposited at a) 10 Pa, b) 20 Pa, c) 50 Pa, d) 70 Pa oxygen pressure. The bar length is 200 nm.

it is possible to induce self-assembly of arrays of hierarchical nanostructures directly from the gas phase. In order to obtain a crystalline film able to efficiently transport charges and to avoid their recombination in lattice traps, it is necessary to heat the as-deposited, amorphous films. On the other hand, annealing induces crystal growth and densification of the nanostructures reducing the specific surface area. In order to optimize the PdO nanostructures for the specific task of this work, a wide range of conditions were explored, namely different background pressures of O_2 (ranging from 10 to 70 Pa) and different post deposition annealing temperatures (from 400 °C to 500 °C).

Figure 3a–d shows scanning electron microscopy (SEM) images for PdO films deposited at different pressure of O_2, 10, 20, 50, and 70 Pa, respectively. A clear trend, similar to the one previously reported for TiO_2,[37,38] can be observed: by increasing the pressure, film morphology evolves from a relatively dense layer at 10 Pa to more porous structures, resembling a forest of nanotrees, up to 50 Pa. Further increase of the deposition pressure leads to the growth of very low density structures with poor mechanical properties. In this work, we focused on the 50 Pa sample, since its open vertical channels guarantee both optimal polymer infiltration and high interaction area with the aqueous electrolyte.

Besides deposition pressure, another critical parameter is the temperature, since it dictates the compromise between the surface area, critical for maximizing electrochemical reactions rate, and the crystallinity, essential for an efficient charge transport. The effect on film morphology of different annealing temperatures has been thus carefully evaluated by SEM (**Figure 4**a–c). Moreover, films crystallinity (deposited at 50 Pa of O_2 pressure) for different annealing temperatures has been quantified by X-ray diffraction (XRD) analysis (Figure 4d). As-deposited films show an amorphous structure, while grain sizes are found to be 11, 15, and 20 nm for films heated at 400 °C, 450 °C, and 500 °C, respectively, as calculated by the Scherrer formula. At temperatures up to 450 °C, a good degree of crystallization is evidenced, without significant, concomitant changes in the

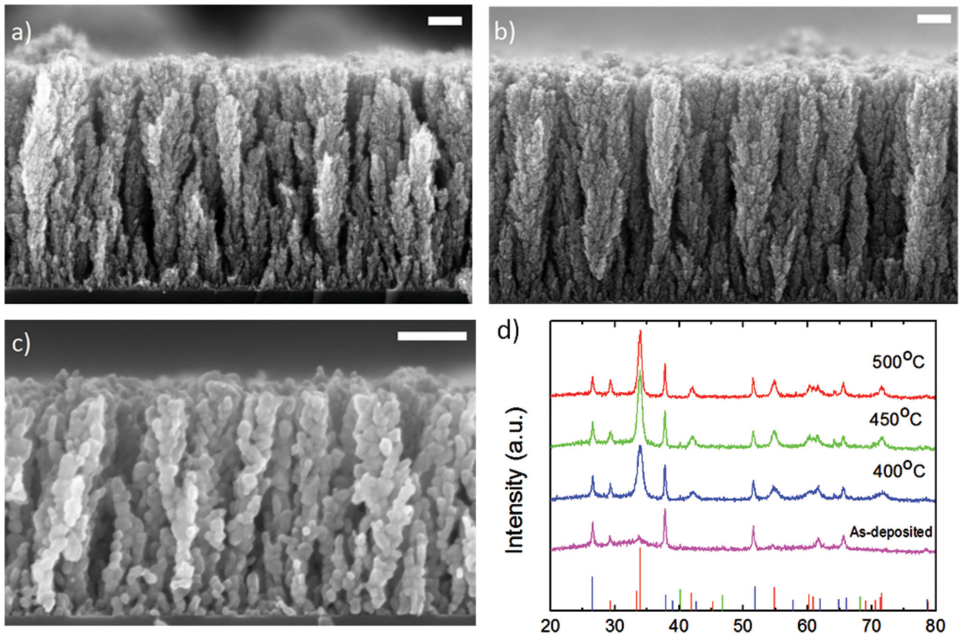

Figure 4. Effect of annealing temperature and oxygen pressure on crystallization. a–c) Effect of the crystallization on the morphology. Cross-section SEM images of crystalline PdO deposited at 50 Pa of O_2 pressure after annealing process at temperature of a) 400 °C, b) 450 °C , c) 400 °C. The bar length is 200 mm. d) XRD data on PdO films deposited at 50 Pa of O_2 pressure deposition annealed at different temperatures.

morphology of the as-deposited films; conversely, above 500 °C big crystals start to form, with a consistent decrease in the available surface area.

In order to verify the charge selectivity behavior of the nanostructures, Kelvin probe measurements were run on as-deposited and annealed samples. Obtained results confirm the hole-selectivity property of the PdO film, with the work function value of 5 and 5.2 eV for the amorphous and crystalline films, respectively. Hence, the crystallized PdO results to be an optimal candidate for a proper hole-selective layer (Figure 2d).

2.3. Photoelectrochemical Dissolved Oxygen Sensor Realization and Characterization

Hybrid devices for oxygen sensing were realized by infiltration of organic film via spin-coating into the PdO matrix. Device optimization was based on the choice of the most efficient organic blend, PLD deposition parameters (pressure, deposition time) and annealing temperature for the PdO nanostructures. Based on SEM and XRD results presented here above, PdO was deposited at 50 Pa O_2 pressure (film thickness, 500 nm) and later annealed at 450 °C.

Figure 5a shows the linear sweep voltammetry (LSV) obtained for different sensors realized with three different polymer blends in PBS at pH 7, namely P3HT:PCBM, MDMO-PPV:PCBM, and APFO-3:PCBM. Bare PdO stability is guaranteed only above 0.1 V vs Ag/AgCl;[33] also in the case of PdO nanostructures cyclic voltammetry experiments showed cathodic peaks below 0.1 V, indicating a reduction process to a metal-like state of PdO (Figure S3, Supporting Information). Linear scan voltammetry (LSV) measurements in dark and upon illumination demonstrate that bare PdO nanostructures do not present intrinsic photocatalytic activity (Figure S3, Supporting Information, right panel). The coverage by the conjugated polymer allows the widening of the stability potential window by few hundreds of mV; however, in order to completely avoid any possible degradation effect, we considered a voltage window just above 0 V vs Ag/AgCl. First of all, differently than in the case of FTO/blend devices (Figure 2), we note the appearance of nonnegligible dark currents, with similar values in all considered polymers, which can be attributed to a capacitive charging occurring at the polymer/electrolyte interface for the scan rate of 5 mV s^{-1}, as a result of the higher specific surface area obtained in the case of nanostructures. In the considered potential range, photocurrent obtained in P3HT:PCBM-based devices is much lower than

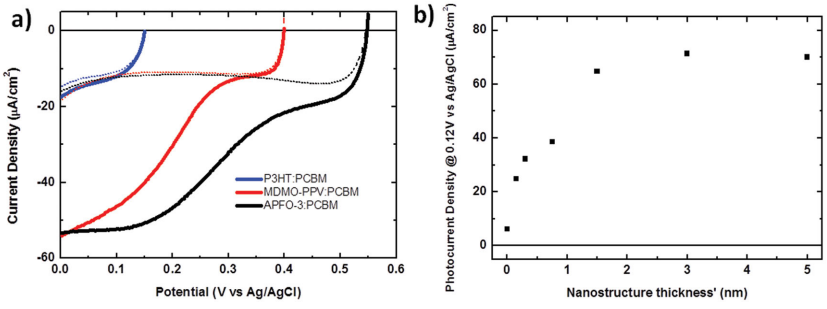

Figure 5. a) Linear sweep voltammetry obtained for different sensors realized with three different blends and 500 nm PdO thick in PBS at pH 7. b) Photocurrent density as a function of PdO film thickness.

the one obtained in the case of MDMO-PPV:PCBM and APFO-3:PCBM. The latter material, in particular, shows photocurrent saturation at ≈0.15 V versus Ag/AgCl. This trend is in agreement with what one could expect from measured OCP values (Figure 2c), thus confirming that, in a specific voltage window, a good compromise between charge generation efficiency and OCP potential must be found. The effect of PdO films thickness on photocurrent density, in the case of APFO-3:PCBM-based device, is shown in Figure 5b. Flat PdO substrate shows photocurrent density comparable to the one obtained by using bare FTO substrates, in the same voltage range (Figure 2), while the introduction of PdO nanostructures resulted in a net performance enhancement, clearly confirming the fundamental role of the nanostructure. Highest photocurrent densities were obtained for a PdO thickness of 3 µm. The good infiltration of the APFO-3:PCBM blend inside the nanostructure, without any capping layer formation, is documented by SEM images (Figure S4, Supporting Information). A further increase of the thickness led to a drop of the performance, possibly due to a progressively poorer polymer infiltration at the bottom part of the nanostructure, together with an increase in the charge recombination probability.

We now turn to better characterize the architecture FTO/PdO/APFO-3:PCBM selected for the realization of the dissolved oxygen sensor, in terms of temporal stability, photoexcitation density, and electrolyte pH value. Chronoamperometry measurements at 0.15 V versus Ag/AgCl (corresponding to maximum photocurrent values), with a dissolved oxygen concentration amounting at 7.5 mg L^{-1} (**Figure 6**a), show excellent stability over more than 2 h continuous operation. The initial photocurrent peak is due to the capacitive current leading to charge accumulation at the FTO/PdO electrode; the response time can be thus estimated in about 20 s after light switch on, needed to reach photocurrent constant values. Dependence on photoexcitation density (Figure 6b) shows a saturation behavior, occurring already above ≈300 µW mm^{-2}. Figure 6c reports preliminary studies on the oxygen reduction reaction of our sensor at different electrolyte pH (1, 4, 7, and 10). The recorded photocurrents are comparable for pH 7 and 10, while they decrease towards similar values for acidic solution (pH 1 and 4). This trend suggests a possible pH dependence on the performance maybe due to different mechanisms leading to ORR, in agreement with Scheme 1 (C1 reactions) and existing reports.[39,40] Detailed characterization of pH dependence, however, deserves a more careful study, currently in progress.

Finally, the realized polymer-based photoelectrochemical dissolved oxygen sensor was properly calibrated, at different oxygen concentrations, by simultaneous measurement with a commercial sensor (**Figure 7**).

The data exhibit the unambiguous correlation between the photocurrent and the oxygen concentration. The fitting procedure resulted in a linear behavior, with $R^2 = 0.987$. Obtained sensitivity is amounting at –5.87 µA cm^{-2}/ppm, comparable to commercial electrochemical sensors, and the detection limit is ≈1.5 mg L^{-1}. Interestingly, the intercept value (–4.85 µA cm^{-2}), reflecting the background signal (obtained by extrapolating the calibration curve to zero, where no oxygen is theoretically present in the solution), is reduced by a 10-fold factor with respect to typical values of commercial Clark electrodes,[41]

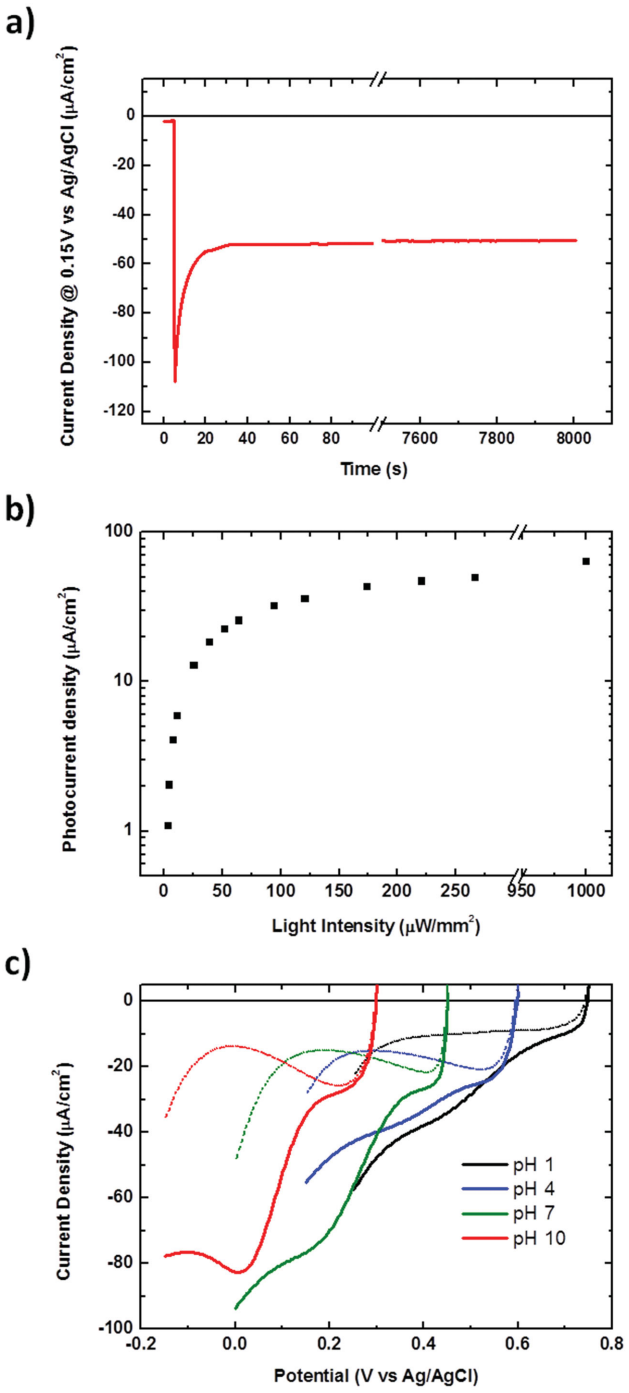

Figure 6. a) Chronoamperometric measurements upon illumination (at 0.15 V vs Ag/AgCl); b) Photocurrent density of the sensor as a function of light intensity; c) Linear scan voltammetry for the hybrid electrode obtained at different pH, in dark (dashed lines) and upon illumination (solid lines).

thus opening the possibility to use our device in all long-term, remote measurements where high signal-to-noise ratios are required and frequent recalibration is not possible. Besides promising performances, it is also worth mentioning that the long-term temporal stability of the device should be explored in

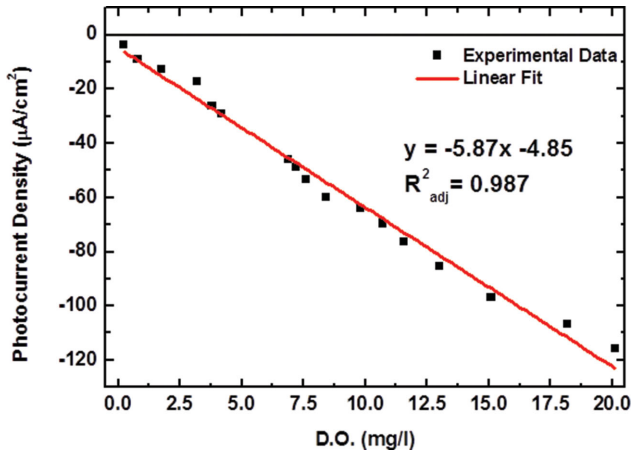

Figure 7. Calibration curve of the realized sensor for dissolved oxygen concentration covering the range between 0 and 20 mg L^{-1}.

more detail. Upon continuous functioning for days or months in harsh environmental conditions, the optoelectronic properties of the polymer layer may degrade, and the polymer thin film, directly exposed to the prolonged contact with the electrolyte, may become mechanically unstable, giving rise to swelling or delamination phenomena, and finally to an overall decrease of its efficiency and reliability. Potential interferences with different concentrations of several components usually present in water, such as ozone, chlorine, and humic acids, should be also carefully evaluated. Moreover, the possibility of up-scaling the device should be carefully evaluated, given the presence of nanostructures. On a lab scale, these can be fabricated at an high throughput efficiency, and easily coupled to the light-sensitive polymer. However, the need for oxygen-sensing areas larger than 10 cm^2 should be more properly addressed by making recourse to other fabrication techniques.

3. Conclusion

We demonstrated successful fabrication of a highly sensitive sensor for dissolved oxygen based on a novel approach, combining visible light sensitivity, optoelectronic properties and easy processability, typical of conjugated polymers with charge selectivity, favorable energetic alignment, and high surface area of PdO nanostructures. Extensive characterization and optimization of the hybrid system have been carried out, based on the screening of several polymers for their ORR photoelectrochemical activity, favorable coupling to specific charge selective oxide, proper choice of optimal parameters in nanostructures fabrication through extensive structural and morphological analysis. Altogether, experimental data led to the successful realization of a highly sensitive sensor for dissolved oxygen, employing non-toxic materials, capable of working in different environmental conditions at different pH values, with good electrochemical and time stability. Notably, background signal is reduced by one order of magnitude with respect to commercial sensors, thus opening the prospects for a wide use in critical conditions, where frequent recalibration and continuous monitoring are not possible.

Besides the demonstration of a practical application in oxygen sensing, results presented in this work are far reaching, since they fully demonstrate the validity of the proposed approach, combining conjugated polymers and inorganic nanostructures, and thus open the way to the realization of different photoelectrochemical devices for several applications in aqueous environment, including biochemical sensing, environmental monitoring, waste water treatment, and water splitting.

4. Experimental Section

Photoelectrode Fabrication: Conjugated polymers screened for their photocatalytic activity include: poly[(9,9-di-n-octylfluorenyl-2,7-diyl)-*alt*-(benzo[2,1,3]thiadiazol-4,8-diyl)] (F8BT), regio-regular poly(3-hexylthiophene-2,5-diyl) (rr-P3HT), poly[2-methoxy-5-(3′,7′-dimethyloctyloxy)-1,4-phenylenevinylene] (MDMO-PPV), poly[*N*-9′-heptadecanyl-2,7-carbazole-alt-5,5-(4,7-di-2-thienyl-2′,1′,3′-benzothiadiazole] (PCDTBT), and poly[(9,9-dioctylfluorenyl-2,7-diyl)-alt-5,5-(4′,7′-di-2-thienyl-2′,1′,3′-benzothiadiazole] (APFO-3). PCBM was used as an electron acceptor in a bulk heterojunction configuration. F8BT and rr-P3HT were purchased from Sigma Aldrich; MDMO-PPV from American Dye Source; PCDTBT from One-Material Inc.; PCBM from Nano-C. All commercial polymers were used without any further purification. APFO-3 was synthesized at Instituto Superior Técnico; synthesis details are reported elsewhere.[42] Polymers were dissolved in proper organic solvents (chlorobenzene for rr-P3HT, and APFO-3; dichlorobenzene for PCDTBT: chloroform for F8BT and MDMO-PPV) and deposited by spin coating on cleaned SnO_2:F (FTO) covered glass substrates (DYESOL, TEC 15, FTO thickness 200 μm, sheet resistance 15 Ω sq^{-1}) or directly on top of the nanostructured PdO network. The solution concentration and the spinning parameters were properly optimized in order to obtain a film thickness in the order of 100–150 nm for deposition on FTO substrates and of few nm for deposition on nanostructured PdO network. The mixture ratio between polymers and PCBM, as well as thermal annealing parameters (not required in some cases), were selected in order to achieve high charge dissociation efficiency, in accordance with existing reports on organic bulk-heterojunction solar cells (rr-P3HT:PCBM and F8BT:PCBM, 1:1 by weight, 140 °C for 10 min and 100 °C for 15 min, respectively, under inert atmosphere; MDMO-PPV:PCBM, PCDTBT:PCBM, and APFO-3:PCBM, 1:4 by weight, no thermal annealing). Nanostructured PdO films in a hyperbranched assembly were directly deposited on FTO-covered glass by means of PLD technique. A Pd target with purity of 99.99% (Testbourne Ltd) was ablated by laser pulses from a KrF excimer laser (wavelength 248 nm pulse duration 20 ns, energy density 2.5 J cm^{-2}, 20 Hz repetition rate) in the presence of O_2 background gas. Morphological factors of the film such as porosity and thickness were carefully controlled by tuning the laser energy, the background gas pressure and the ablation time and frequency. As-produced films underwent an annealing procedure in a muffle oven furnace in presence of air to achieve fully crystalline structure. Different annealing temperatures were tested, in the range of 400 °C–500 °C. Photocatalytic electrodes (active area, 1 cm^2) were immersed at room temperature (22 °C) in different saline aqueous solutions, characterized by different pH values. In particular, we used: hydrochloric acid-potassium chloride buffer (HCl/KCl buffer, obtained by mixing 50 mL of 0.2 M KCl and 97 mL of 0.2 M HCl, and then diluting to a volume of 200 mL with distilled water) for pH 1. Acetate buffer (obtained by mixing 41 mL of 0.1 M $C_2H_4O_2$ and 9 mL of 0.1 M $C_2H_3O_2Na$, and then adjusting the final volume to 100 mL with deionized water) for pH 4. Sodium phosphate buffer (obtained by mixing 39 mL of 0.1 M NaH_2PO_4) and 61 mL of 0.1 M Sodium phosphate bibasic (Na_2HPO_4) and adjusting the final volume to 200 mL with deionized water) for pH 7. Carbonate–bicarbonate buffer (obtained by mixing 27.5 mL of 0.1 M $NaHCO_3$ and 22.5 mL of Na_2CO_3, and adjusting the final volume to 200 mL with deionized water) for pH 10.

Material Characterization: Absorbance spectra were recorded by using a spectrophotometer (PerkinElmer, Lambda 1040) in transmission and reflectance mode. SEM (Zeiss SUPRA 40) images from top and cross-sectional views of the samples served to characterize the morphology and the thickness of the PLD-grown films. Crystallinity of PdO nanostructures was characterized by XRD by means of an automatic diffractometer for powders (Philips X' Pert) in $\theta/2\theta$ grazing angle geometry, with incidence angle (θ) fixed to 1°, using CuKθ radiation X with $\lambda = 1.5416$ Å and power 1.6 kW. The angular range used for 2θ was from 5° to 90° with steps of 0.02° and acquisition time 5 s per step. Work function data were obtained by using a Kelvin Probe Microscope (Bruker, Dimension Icon) in air and at room temperature. A reference sample of graphite (HOPG, highly ordered pyrolytic graphite) was used for calibration, as its work function value (4.6 eV) is well determined.

Photoelectrical and Photoelectrochemical Measurements: Electrochemical characterization was carried out by using a potentiostat/galvanostat (Autolab, PGSTAT 302N), in a three-electrode configuration. Ag/AgCl in a saturated KCl solution and a Pt wire were used as a reference and counter electrode, respectively. Linear sweep voltammetry (LSV) was performed with a scan rate of 5 mV s^{-1}. Light source consisted in a Class AAA solar simulator (Oriel, Model 94063A) simulating the AM1.5G spectrum. Photoexcitation density was in the order of 100 mW cm^{-2}. For intensity dependence measurements, a collimated white LED (MCWHL2-C4, Thorlabs) was used, in a range between 5 nW cm^{-2} and 2.70 μW cm^{-2}. Calibration of the oxygen sensors was performed by measuring the photocurrent density at several dissolved oxygen concentrations (0.2–22 mg L^{-1}) by purging N_2 and O_2 in the aqueous solution. The process was monitored through a commercial dissolved oxygen sensor (CRISON Oxygen meter, OXI 45+).

Supporting Information

Supporting Information is available from the Wiley Online Library or from the author.

Acknowledgements

S.B. and A.G. equally contributed to this work. The authors acknowledge the financial support of the European Community through the Future and Emerging Technologies (FET) programme under the FP7, Collaborative Project contract n° 309223 (PHOCS).

Received: February 19, 2015
Revised: May 19, 2015
Published online: June 16, 2015

[1] M. L. Hichman, *The Measurement of Dissolved Oxygen*, Wiley, New York **1978**.
[2] X.-D. Wang, O. S. Wolfbeis, *Chem. Soc. Rev.* **2014**, *43*, 3666.
[3] C. Mc Donagh, C. Kolle, A. K. McEvoy, D. L. Dowling, A. A. Cafolla, S. J. Cullen, B. D. Mac Craith, *Sens. Actuators B* **2001**, *74*, 124.
[4] D. Zhang, Y. Fang, Z. Miao, M. Ma, *J. Appl. Electrochem.* **2014**, *44*, 419.
[5] J.-M. Zen, Y.-S. Song, H.-H. Chung, C.-T. Hsu, A. S. Kumar, *Anal. Chem.* **2002**, *74*, 6126.
[6] G. Bencsik, Z. Lukács, C. Visy, *Analyst* **2010**, *135*, 375.
[7] W. Wang, L. Bao, J. Lei, W. Tu, H. Ju, *Anal. Chim. Acta* **2012**, *744*, 33.
[8] Z. Yue, F. Lisdat, W. J. Parak, S. G. Hickey, L. Tu, N. Sabir, D. Dorfs, N. C. Bigall, *ACS Appl. Mater. Interfaces* **2013**, *5*, 2800.
[9] A. Köhler, H. Bässler, *Electronic Processes in Organic Semiconductors*, Wiley-VCH Verlag, Weinheim, Germany **2015**.
[10] S. Esiner, H. van Eersel, M. M. Wienk, R. A. J. Janssen, *Adv. Mater.* **2013**, *25*, 2932.
[11] I.-S. Shin, T. Hirsch, B. Ehrl, D.-H. Jang, O. S. Wolfbeis, J.-I. Hong, *Anal. Chem.* **2012**, *84*, 9163.
[12] E. Lanzarini, M. R. Antognazza, M. Biso, A. Ansaldo, L. Laudato, P. Bruno, P. Metrangolo, G. Resnati, D. Ricci, G. Lanzani, *J. Phys. Chem. C* **2012**, *116*, 10944.
[13] G. Suppes, E. Ballard, S. Holdcroft, *Polym. Chem.* **2013**, *4*, 5345.
[14] D. Ghezzi, M. R. Antognazza, M. Dal Maschio, E. Lanzarini, F. Benfenati, G. Lanzani, *Nat. Commun.* **2011**, *2*, 166.
[15] D. Ghezzi, M. R. Antognazza, R. Maccarone, S. Bellani, E. Lanzarini, N. Martino, M. Mete, G. Pertile, S. Bisti, G. Lanzani, F. Benfenati, *Nat. Photonics* **2013**, *7*, 400.
[16] A. Guerrero, M. Haro, S. Bellani, M. R. Antognazza, L. Meda, S. Gimenez, J. Bisquert, *Energy Environ. Sci.* **2014**, *7*, 3666.
[17] S. Bellani, D. Fazzi, P. Bruno, E. Giussani, E. V. Canesi, G. Lanzani, M. R Antognazza, *J. Phys. Chem. C* **2014**, *118*, 6291.
[18] B. Winther-Jensen, D. R. MacFarlane, *Energy Environ. Sci.* **2011**, *4*, 2790.
[19] T. Bourgeteau, D. Tondelier, B. Geffroy, R. Brisse, C. Laberty-Robert, S. Campidelli, R. de Bettignies, V. Artero, S. Palacina, B. Jousselme, *Energy Environ. Sci.* **2013**, *6*, 2706.
[20] G. Wu, K. L. More, C. M. Johnston, P. Zelenay, *Science* **2011**, *332*, 443.
[21] K. Lee, L. Zhang, H. Lui, R. Hui, Z. Shi, J. Zhang, *Electrochim. Acta* **2009**, *54*, 4704.
[22] V. G. Khomenko, V. Z. Barsukov, A. S. Katashinskii, *Electrochim. Acta* **2005**, *50*, 1675.
[23] O. Madelung, U. Rössler, M. Schulz, *Landolt-Börnstein – Group III Condensed Matter*, Springer, Berlin-Heidelberg, Berlin, Germany **2000**.
[24] M. K. Bruska, I. Czekaj, B. Delley, J. Mantzaras, A. Wokaun, *Phys. Chem. Chem. Phys.* **2011**, *13*, 15947.
[25] C.-J. Huang, F.-M. Pan, H.-Y. Chen, L. Chang, *J. Appl. Phys.* **2010**, *108*, 053105.
[26] T. Arai, T. Shima, T. Nakano, J. Tominaga, *Thin Solid Films* **2007**, *515*, 4774.
[27] R. Baca-Arroyo, C. A. Lopez Rodriguez, M. Galvan-Arellano, G. Romero-Paredes, R. Pena-Sierra, *ICEEE* **2007**, *2007*, 345.
[28] J. Zhang, *PEM Fuel Cell Electrocatalysts and Catalysts Layer*, Springer, London **2008**.
[29] A. Haugeneder, M. Neges, C. Kallinger, W. Spirkl, U. Lemmer, J. Feldmann, U. Scherf, E. Harth, A. Gügel, K. Müllen, *Phys. Rev. B* **1999**, *59*, 15346.
[30] P. E. Shaw, A. Ruseckas, I. D. W. Samuel, *Adv. Mater.* **2008**, *20*, 3516.
[31] G. Dennler, M. C. Scharber, C. J. Brabec, *Adv. Mater.* **2009**, *21*, 1323.
[32] R. Steim, F. R. Kogler, C. J. Brabec, *J. Mater. Chem.* **2010**, *20*, 2499.
[33] N. Takeno, *Atlas of E_H - pH Diagrams* Intercomparison of thermodynamic databases, Geological Survey of Japan Open File Report No.419, National Institute of Advanced Industrial Science and Technology **2005**.
[34] R. K. Singh, J. Narayan, *Phys. Rev. B* **1990**, *41*, 8843.
[35] V. Dolique, A.-L. Thomann, E. Millon, A. Petit, P. Brault, *Appl. Surf. Sci.* **2014**, *295*, 194.
[36] D. Dellasega, A. Facibeni, F. Di Fonzo, M. Bogana, A. Polissi, C. Conti, C. Ducati, C. S. Casari, A. Li Bassi, C. E. Bottani, *Nanotechnology* **2008**, *19*, 475602.
[37] F. Sauvage, F. Di Fonzo, A. Li Bassi, C. S. Casari, V. Russo, G. Divitini, C. Ducati, C. E. Bottani, P. Comte, M. Graetzel, *Nano Lett.* **2010**, *10*, 2562.
[38] L. Passoni, F. Ghods, P. Docampo, A. Abrusci, J. Marti-Rujas, M. Ghidelli, G. Divitini, C. Ducati, M. Binda, S. Guarnera, A. Li Bassi, C. S. Casari, H. J. Snaith, A. Petrozza, F. Di Fonzo, *ACS Nano* **2013**, *7*, 10023.
[39] N. Ramaswamy, S. Mukerjee, *Adv. Phys. Chem.* **2012**, *2012*, 1.
[40] M. F. Li., L. W. Liao, D. F. Yuan, D. Mei, Y.-X. Chen, *Electrochem. Acta* **2013**, *110*, 780.
[41] G. Koley, J. Liu, M. W. Nomani, M. Yim, X. Wen, T.-H. Hsia, *Mater. Sci. Eng. Rep.* **2009**, *29*, 685.
[42] R. Rodrigues, R. Meira, Q. Ferreira, A. Charas, J. Morgado, *Materials* **2014**, *7*, 8189.